Nanoscale

ROYAL SOCIETY OF CHEMISTRY

PAPER

View Article Online
View Journal

Check for updates

Cite this: DOI: 10.1039/d4nr05278a

Photoactivated defect engineering and nanostructure functionalization of MoS_2 *via* a photochemical Fenton process†

Tuan-Hoang Tran,[a] Raul D. Rodriguez, *[a] Aura Garcia,[a] Qiang Ma,[b] Tao Zhang,[b] Ranran Wang[c] and Evgeniya Sheremet[a]

Molybdenum disulfide (MoS_2) is a promising 2D material for (photo)catalysis. However, its performance in (photo)catalytic applications is usually limited by a small amount of catalytically active defects. Here, we developed a novel large-scale, rapid, green, low-cost photoetching technique to transform multilayer MoS_2 into a few-layer MoS_2 with high defect density and simultaneous spatial functionalization of MoS_2 with magnetic nanostructures using a photo-driven Fenton reaction. The photoetching process and resulting nanostructures were characterized by optical microscopy, atomic force microscopy, photoluminescence, and Raman spectroscopy. We elucidated the reaction mechanism driven by the Fenton reaction in which photogenerated charge carriers in MoS_2 play a dual role: reducing Fe^{3+} and Cu^{2+} ions and generating hydrogen peroxide (H_2O_2) from water and dissolved O_2. In this Fenton reaction, Fe^{2+} ions react with H_2O_2 to generate hydroxyl ($^{\bullet}OH$) radicals, oxidizing MoS_2 and forming metal oxide nanostructures at the reaction sites. This dual pathway, triggered by MoS_2 photon absorption even at low-intensity illumination, ensures *in situ* generation of Fenton reactants (Fe^{2+} and H_2O_2), generating $^{\bullet}OH$, to achieve on-demand thinning and functionalization of MoS_2 in a single step. Electron paramagnetic resonance spectroscopy confirmed the generation of $^{\bullet}OH$ radicals as the main reactive oxygen species. This photochemical approach enables the photo-driven creation and growth of defects from submicrometer regions up to a dozen micrometers, both at native defects and predefined defective region seeds, by photochemical processing of MoS_2 in $FeCl_3$ and $CuSO_4$ solutions. The presence of metal oxide nanostructures on MoS_2 was verified using magnetic force microscopy, scanning electron microscopy with elemental mapping by energy dispersive X-ray spectroscopy and Raman spectroscopy. The simultaneous photoetching and metal oxide deposition improves the catalytic performance of MoS_2 in the electrical hydrogen evolution reaction, evidenced by a potential shift from −0.7 V (graphite electrode) to −0.47 V (MoS_2 sample photoetched in $FeCl_3$ solution under a halogen lamp illumination) at a current density of 10 mA cm^{-2}.

Received 14th December 2024,
Accepted 6th April 2025

DOI: 10.1039/d4nr05278a

rsc.li/nanoscale

1. Introduction

Molybdenum disulfide (MoS_2) is the most studied 2D semiconductor material, known for its unique properties, such as emerging photoluminescence in its monolayer form[1] and its potential in next-generation applications such as photovoltaics,[2] energy storage,[3] photon detection,[4] and (photo)catalysis.[5] In (photo)catalysis, defect engineering in MoS_2 opens new avenues for tailoring its physical and electronic properties to enhance its performance.[6,7] For instance, MoS_2 edges (defects) are catalytically active sites for the hydrogen evolution reaction (HER), with near zero Gibbs free energy;[8] consequently, increasing the defect concentration improves HER efficiency.[9] However, large-scale, low-cost, and environmentally friendly production of thin MoS_2 with high defect density remains a challenge. Various bottom-up and top-down approaches have been developed to synthesize thin MoS_2 with high defect density (Table S1†). Among bottom-up methods, wet chemical synthesis offers control over surface morphology, crystallite size, and doping but faces scalability issues due to size and thickness inhomogeneity and harsh conditions (*e.g.*,

[a]*Tomsk Polytechnic University, Lenina Avenue, 30, 634050 Tomsk, Russia. E-mail: raul@tpu.ru*
[b]*Key Laboratory of Marine Materials and Related Technologies, Ningbo Institute of Materials Technology and Engineering, Chinese Academy of Sciences, Ningbo 315201, China*
[c]*Shanghai Institute of Ceramics, Chinese Academy of Sciences, Shanghai, China*
† Electronic supplementary information (ESI) available. See DOI: https://doi.org/10.1039/d4nr05278a

high pressure and hazardous chemical agents).[10] In the top-down approaches, chemical liquid exfoliation can achieve high defect density under ambient conditions but suffers from non-uniform thickness and poor production yield, limiting large-scale production. Other conventional top-down techniques like laser thinning in air and plasma treatment[11–13] struggle with scalability, cost, and safety.[9]

Here, we introduced a single-step, scalable, cost-effective, and environmentally friendly method for thinning and functionalization of MoS_2 in an aqueous solution using a light-driven Fenton reaction with $FeCl_3$ or $CuSO_4$ solutions alone. Unlike traditional Fenton processes, this approach does not require external supplies of Fe^{2+} or H_2O_2 as they are produced in the system under light illumination. In this process, the production of hydroxyl radicals ($^{\bullet}OH$) generated by the Fenton reaction enables the etching of multilayer to few-layer MoS_2 with high defect density and simultaneously forming metal oxide nanostructures on MoS_2. The spatial control of the etching and metal oxide deposition area can be achieved by laser processing technology in the air and by adjusting light intensity and illumination time. Incorporating defects and metal oxide nanoparticles enhances the catalytic activity of multilayer MoS_2 for the HER, demonstrating the versatility and potential for creating new MoS_2-based materials with added functionalities.

2. Results and discussion

2.1. Boosting ROS production by the Fenton reaction with $FeCl_3$ for MoS_2 photoetching

It is known that MoS_2 is thinned through oxidation in water by reactive oxygen species (ROS), such as superoxide radicals ($^{\bullet}O_2^-$) and $^{\bullet}OH$.[14] This process can be described by the following reactions (1) and (2):[15]

$$MoS_2 + 6^{\bullet}O_2^- \rightarrow MoO_4^{2-} + 2SO_4^{2-} \quad (1)$$

$$MoS_2 + 18^{\bullet}OH \rightarrow MoO_4^{2-} + 2SO_4^{2-} + 6H_2O + 6H^+ \quad (2)$$

However, Ghim *et al.* reported that only 0.21% of MoS_2 with a thickness of 18 nm dissolves in water after 24 hours of exposure to simulated sunlight,[14] highlighting the need for efficient ROS generation methods for rapid and effective etching of multilayer MoS_2 to few-layer MoS_2 with high defect density.

Advanced oxidation processes (AOPs), including chemical, photochemical, and electrochemical methods, have been developed to effectively generate strongly oxidizing ROS.[16] The Fenton reaction is the most commonly used AOP method, producing strong $^{\bullet}OH$ radicals according to the following eqn (3) and (4), with the reaction rate constant k:

$$Fe^{2+} + H_2O_2 \rightarrow Fe^{3+} + OH^- + {}^{\bullet}OH, \quad k = 51\ M^{-1}\ s^{-1} \quad (3)$$

$$Fe^{3+} + H_2O_2 \rightarrow Fe^{2+} + {}^{\bullet}O_2^- + 2H^+, \quad k = 2 \times 10^{-3}\ M^{-1}\ s^{-1} \quad (4)$$

The low reaction rate of Fe^{3+} with hydrogen peroxide (H_2O_2) (eqn (4)) and the low regeneration rate of Fe^{2+} from Fe^{3+} limit the Fenton reaction, hindering the overall ROS regeneration efficiency. This is why the Fenton reaction requires substantial amounts of Fe^{2+} and H_2O_2 to achieve effective oxidation.[17] For instance, industrial applications typically require high concentrations of Fe^{2+} (18–410 mmol L^{-1}) and H_2O_2 (30–6000 mmol L^{-1}) to generate sufficient $^{\bullet}OH$ for practical use.[18]

Several strategies can be adapted to address the issues of Fe^{2+} regeneration and high Fe^{2+} and H_2O_2 consumption. One of the most promising methods is using semiconductors in photocatalytic water-splitting reactions. For instance, semiconductors can directly reduce Fe^{3+} to Fe^{2+} through photogenerated electrons or *via* $^{\bullet}O_2^-$ (eqn (5)), generated in photocatalytic water-splitting reactions. Furthermore, $^{\bullet}O_2^-$ can generate H_2O_2 (eqn (6)), which is critical for driving the Fenton reaction.[19]

$$Fe^{3+} + {}^{\bullet}O_2^- \rightarrow Fe^{2+} + O_2, \quad k = 7.8 \times 10^5\ M^{-1}\ s^{-1} \quad (5)$$

$$2H^+ + e^- + {}^{\bullet}O_2^- \rightarrow H_2O_2, \quad k = 2.3 \times 10^6\ M^{-1}\ s^{-1} \quad (6)$$

Therefore, semiconductor photocatalysts can address both the challenges of Fe^{2+} regeneration and the high consumption of Fe^{2+} and H_2O_2. To harvest solar energy, the photocatalyst has to possess a small band gap. With its low band gap of 1.3 eV,[5] multilayer MoS_2 is emerging as a promising candidate for solving Fenton-reaction issues and potentially boosting ROS generation in this reaction through photocatalysis under visible irradiation. Recently, Fe^{2+} regeneration from Fe^{3+} was significantly enhanced by adding Fe-doping oligo-layer natural molybdenite as a cocatalyst to the Fenton system.[20] It is also reported that H_2O_2 is produced effectively by MoS_2 in photocatalytic water-splitting reactions.[21] Thus, we hypothesize that promoting the effective ROS generation based on the Fenton-reaction is possible by illuminating MoS_2 in $FeCl_3$ without the need for external addition of Fe^{2+} and H_2O_2.

To verify our hypothesis, we performed the irradiation of MoS_2 on highly oriented pyrolytic graphite (HOPG) in water and aqueous 1 mM $FeCl_3$ solution using a 532 nm laser at a power of 0.1 mW through a 100× objective in 10 seconds. Fig. 1(a) and (b) show the optical images of MoS_2 on HOPG before and after laser irradiation in distilled water where the etched area presents as a dark spot. The MoS_2 is photoetched in water with a low laser power of 0.1 mW (power density ~2×10^4 W cm^{-2}), which is approximately 100 times lower than the photoetching threshold in air.[22] These results suggest that MoS_2 can be photoetched more effectively in water than in air. After laser irradiation of MoS_2 in $FeCl_3$ solution with the same parameters, the etching of MoS_2 is further enhanced, affecting the whole flake (see Fig. 1(c) and (d)). The large etching area within a short irradiation time (10 seconds) and with a low laser power (0.1 mW), which is significantly larger than the

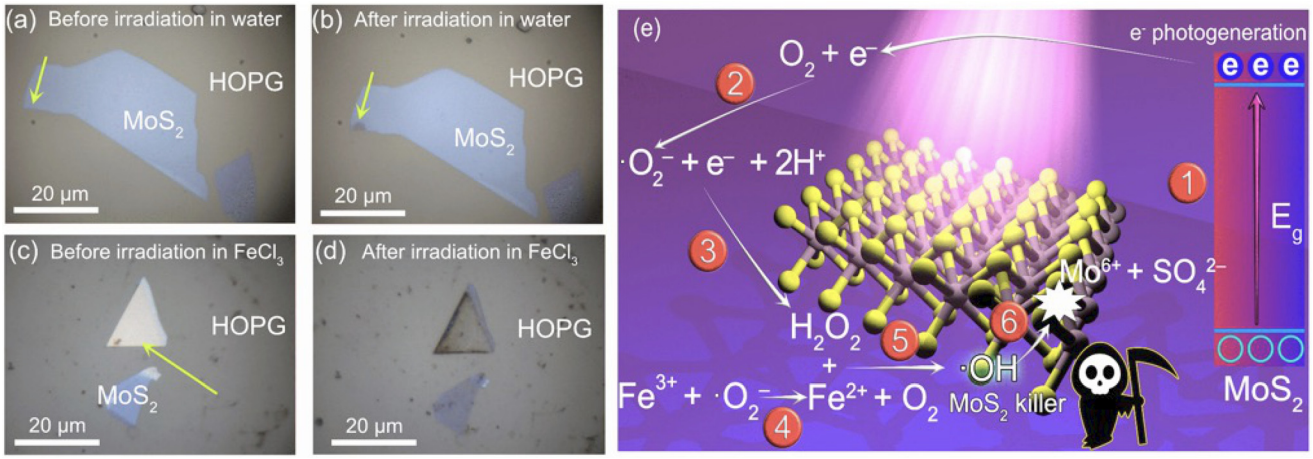

Fig. 1 Optical image of MoS_2 on HOPG: (a) before and (b) after laser irradiation in distilled water using a 532 nm laser at the power of 0.1 mW through a 100× objective in 10 seconds; and (c) before and (d) after laser irradiation in 1 mM $FeCl_3$ using a 532 nm laser at the power of 0.1 mW through a 100× objective in 10 seconds. (The arrows show the irradiated spots). (e) Schematic illustration of the photoetching mechanism of MoS_2 in $FeCl_3$ under illumination, highlighting ROS generation and the Fenton reaction for controlled etching.

laser beam diameter (~800 nm), suggests the potential of our method for the scalable production of thin MoS_2.

The schematic mechanism of MoS_2 photoetching in $FeCl_3$ under illumination is presented in Fig. 1(e):

(1) Photon absorption by MoS_2 generates free electrons (e^-) and holes (h^+).

(2) Dissolved O_2 reacts with photogenerated e^- to produce $^{\bullet}O_2^-$.

(3) $^{\bullet}O_2^-$ further reacts with electrons and protons (H^+) to produce H_2O_2 and OH^- (see eqn (6)). This process provides the H_2O_2 needed to fuel the Fenton reaction.

(4) The Fe^{2+} necessary to trigger the Fenton reaction is generated either by the reduction of Fe^{3+} through superoxide radicals (see eqn (5)) or directly by photoexcited electrons in MoS_2.

(5) The Fenton reaction occurs when Fe^{2+} reacts with the H_2O_2 generated by MoS_2, producing Fe^{3+} and $^{\bullet}OH$ radicals as products (see eqn (3)).

(6) These strongly oxidizing $^{\bullet}OH$ radicals attack MoS_2, resulting in the formation of Mo^{6+} and sulfate (SO_4^{2-}) ions. Consequently, ROS production and photoetching are significantly enhanced due to the generation of highly oxidizing $^{\bullet}OH$ radicals[23] (see eqn (1)).

As long as MoS_2 and a light source are present, photoexcited charge carriers are generated and the system will continue to produce H_2O_2 and Fe^{2+}. This allows the Fenton reaction to continue without Fe^{2+}, H_2O_2 consumption and Fe^{2+} regeneration issues.

To confirm the generation of the $^{\bullet}OH$ radical, we performed electron paramagnetic resonance (EPR) spectroscopy. The increase in the EPR signal of the $^{\bullet}OH$ radical after irradiation of MoS_2 in the $FeCl_3$ solution confirms the enhanced generation of $^{\bullet}OH$ in our system and validates the photo-driven Fenton mechanism (see Fig. S1 and the explanation in the ESI†).

To visualize the effect of $^{\bullet}OH$ radicals on MoS_2 photoetching, we conducted $^{\bullet}OH$ quenching experiments using isopropyl alcohol (IPA) as a $^{\bullet}OH$ scavenger. A halogen lamp was employed as the light source for better visualization. The results presented in Fig. S2† show no observable change after immersing in $FeCl_3$ and $FeCl_3$ + IPA solution, confirming the absence of any spontaneous reaction between MoS_2 and $FeCl_3$ or $FeCl_3$ + IPA. Using high-magnification optical microscopy, we quantified the etched area of MoS_2 in $FeCl_3$ + IPA to be about 14 μm^2. This etched area was smaller than the 33 μm^2 obtained in $FeCl_3$ without IPA. The difference in the photoetching area is even more pronounced when considering that the illumination time was 2 minutes for the $FeCl_3$ solution with IPA, compared to just 10 seconds without IPA. These results demonstrate the quenching effect due to the addition of IPA as a hydroxyl radical scavenger, confirming our hypothesis of $^{\bullet}OH$-driven photoetching of MoS_2.

Further evidence for the Fenton reaction was provided by monitoring the pH of dispersions containing MoS_2, $FeCl_3$, and MoS_2 with $FeCl_3$, with and without illumination of halogen lamps for 2 hours. The results showed that the pH decrease in the MoS_2 + $FeCl_3$ solution after halogen lamp illumination for 2 hours was smaller than the sum of the pH decreases in the MoS_2 and $FeCl_3$ solutions individually (see Table S2†). This observation indicates the generation of OH^- ions during the Fenton reaction, which partially offset the H^+ ions generated by MoS_2 and $FeCl_3$. The presence of OH^- supports the proposed Fenton reaction mechanism (eqn (3)), which includes OH^- and $^{\bullet}OH$ as products.

Finally, we also ruled out $^{\bullet}Cl$ radicals as the main driving force for photoetching since repeating the experiment in a NaCl solution yielded no observable changes (see Fig. S3†).

The laser power density of ~2×10^4 W cm^{-2} in our photoetching experiment is much higher than the power density of solar irradiation on the Earth's surface (~0.14 W cm^{-2}). To

illustrate the use of visible light for large-scale, green, and low-cost photoetching, we used a halogen lamp as the light source with an emission spectrum as shown in Fig. S4.† We still observed effective photoetching of MoS_2 in the $FeCl_3$ solution under halogen lamp illumination with a power of 22.5 W, as shown in the optical images and photoluminescence (PL) intensity maps (Fig. 2(a)–(d)). The noticeable change in the flake color of MoS_2 from blue to gray, similar to that of HOPG, and the increase in PL intensity indicate the effective photoetching of MoS_2 to a few-layer structure. This color change occurs because few-layer MoS_2 exhibits low light absorption, reduced optical contrast compared to HOPG,[24] and high PL emission. In contrast, control experiments under dark conditions showed no etching of MoS_2 by $FeCl_3$ (see Fig. S5†), confirming the absence of a spontaneous reaction and the crucial role of light in the photoetching process. As proposed in the mechanism, light is necessary to produce photoexcited electrons in MoS_2, which are essential for generating $^{\bullet}O_2^-$, H_2O_2 and Fe^{2+} for the Fenton reaction. The results in Fig. S6† show that no etching of MoS_2 occurred in distilled water under halogen lamp illumination, likely because the low power density of the halogen lamp and short illumination time were insufficient to induce visible etching.

The normalized PL spectra of pristine mechanically exfoliated monolayer, photoetched at location 1, and multilayer MoS_2 samples reveal significant PL intensity enhancement, a blue shift, and peak broadening at location 1. The PL spectra were normalized to the E^1_{2g} Raman peak of MoS_2. In the photoetched regions, the PL intensity increases significantly, consistent with the thinning of MoS_2 and a reduction in layer

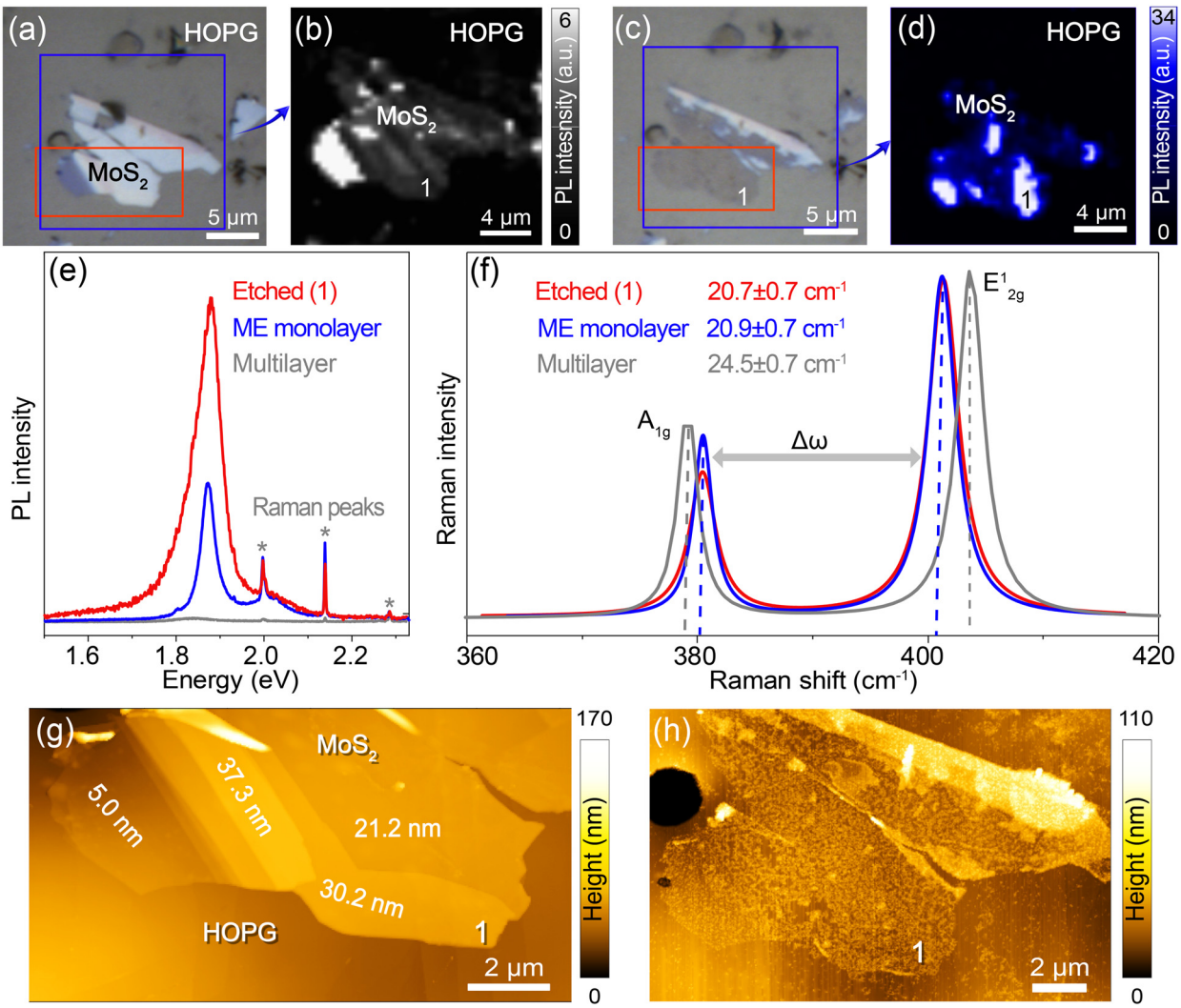

Fig. 2 (a)–(d) Optical (a and c) images and PL intensity maps (b and d) of MoS_2 before (a and b) and after (c and d) photoetching in $FeCl_3$ under halogen lamp illumination, showing enhanced PL intensity in the etched area consistent with layer thinning. (e) Photoluminescence (PL) spectra of mechanically exfoliated (ME) monolayer, multilayer, and etched MoS_2 at point (1) in (c) and (d) showing increased intensity after photoetching, and (f) mechanically exfoliated monolayer, multilayer, and etched MoS_2 at point (1) in (c) and (d), where the peak position difference ($\Delta\omega$) confirms monolayer thickness after photoetching. (g) AFM height profile of multilayer MoS_2 flakes on HOPG before photoetching, showing thicknesses ranging from 5 nm to 37.3 nm. (h) AFM image of MoS_2 after photoetching, revealing surface modifications.

thickness.[1] The blue shift and a broadening PL peak could be explained by the created defects or nanoparticles or by doping MoS_2 during photoetching.[25,26] Our results align with a previous study,[25] demonstrating the blue shift in PL by defect engineering and oxygen bonding. The broadening of the PL peak could be due to the formation of the metal oxide after photoetching,[27] as suggested by EDX results in Fig. S7.† Fig. S8 and S9† show the PL spectra before and after photoetching. The 28-fold and 7-fold enhancement in PL intensity after photoetching clearly demonstrates the thinning of MoS_2 down to a few layers or monolayers[1] and an increase in the defect density[25] after halogen lamp illumination in $FeCl_3$.

To investigate the effect of layer thickness on photoetching, we illuminated mechanically exfoliated (ME) multilayer and few-layer MoS_2 in $FeCl_3$. No changes were evidenced in optical microscopy imaging of few-layer MoS_2, in contrast to the observations for multilayer MoS_2 (Fig. S10†). These results show that the photoetching rate decreases when MoS_2 is thinned to a few layers, suggesting a new pathway to control layer thickness based on light absorption without the need for an applied potential bias, unlike the electrochemical conditions used in a previous report.[28] The reason for this effect is the low light absorption in the visible range of few-layer MoS_2 compared to its bulk form.[29] Another reason could be that fast charge recombination in few-layer MoS_2, as evidenced by strong PL,[28] reduces the amount of $^{\bullet}OH$ radicals, leading to less effective photoetching of MoS_2.

It is well known that the peak position difference between E^1_{2g} (in-plane vibrations of Mo and S atoms) and A_{1g} (out-of-plane vibrations of S atoms) allows for the evaluation of layer thickness.[30] Therefore, we recorded the Raman spectra of ME MoS_2 and MoS_2 after photoetching. The results are shown in Fig. 2(f). The peak position difference between E^1_{2g} and A_{1g} for both ME monolayer MoS_2 and photoetched MoS_2 at point 1 are identical, at $\approx 20.9 \pm 0.7$ cm^{-1}, confirming the presence of monolayer MoS_2 after photoetching. This value is significantly smaller than 24.5 ± 0.7 cm^{-1} for multilayer MoS_2, confirming the photoetching of multilayer MoS_2. Additionally, the E^1_{2g} peak width of etched MoS_2 at point 1 is 2.9 ± 0.4 cm^{-1}, which is higher than the value of ME monolayer MoS_2 (1.98 ± 0.4 cm^{-1}). The A_{1g} peak width of photoetched MoS_2 at point 1 is 3.29 ± 0.4 cm^{-1} compared to 2.90 ± 0.4 cm^{-1} for ME monolayer MoS_2. These results demonstrate defect introduction to MoS_2 during photoetching, consistent with previous reports of MoS_2 Raman peaks widening due to defects.[31,32]

Fig. 2(g) shows the atomic force microscopy (AFM) image of multilayer MoS_2 flakes on HOPG before photoetching, with thicknesses ranging from 5 nm to 37.3 nm. Fig. 2(h) presents the AFM image of MoS_2 after photoetching in $FeCl_3$ under illumination, highlighting significant surface modifications of the MoS_2 flakes. However, due to nanoparticles on the MoS_2 surface, we could not precisely determine the layer thickness. These nanoparticles significantly increase the surface roughness, which could be advantageous for applications like hydrogen production.[9] For instance, the root mean square surface roughness of MoS_2 flakes with thicknesses of 5.0 ± 0.1 nm and 21.3 ± 0.1 nm increased from 1.8 ± 0.2 nm and 0.6 ± 0.2 nm to 4.4 ± 0.6 nm and 5.1 ± 0.9 nm, respectively. This increase in surface roughness can be related to nanoparticle formation or high defect concentration, evidenced by Raman spectroscopy.

Additional experiments were performed on MoS_2 flakes deposited on Si/SiO_2 in $FeCl_3$. We still observed MoS_2 photoetching (see Fig. S11†), which shows the applicability of our approach regardless of the substrate. However, the photoetching efficiency of MoS_2 on HOPG is most effective[33,34] (see Fig. S12†), which can be explained.

In summary, we demonstrated a rapid, green, low-cost etching method for production of thin MoS_2 with high defect density and nanoparticle deposition by simply illuminating MoS_2 in $FeCl_3$ solution using a halogen lamp with a low light intensity. The photoetching efficiency is closely linked to the generation of photoexcited charge carriers in MoS_2, producing ROS in the photocatalytic water splitting reaction and $^{\bullet}OH$ in the Fenton reaction. Therefore, the presence of photoexcited charges in MoS_2 is critical, as evidenced by the slower photoetching rate of few-layer MoS_2 compared to multilayer MoS_2, attributed to lower light absorption or faster charge recombination and no change in the optical image of MoS_2 after immersing in $FeCl_3$ in dark.

2.2. Spatially controlled photoetching and nanostructuring on laser-engineered defects on MoS_2

Previous research indicates that MoS_2 oxidation–dissolution or particle deposition typically initiates at the edges due to their defective nature.[35–37] Our previous work demonstrated spontaneous deposition of Ag nanostructures at laser-carved defects on MoS_2 without illumination,[22] motivating us to control MoS_2 photoetching and nanoparticle growth at laser-engineered defects. We observed that photoetching of MoS_2 in $FeCl_3$ solution initiates at the defects or edges (see Fig. S10†).

Laser processing technology offers the advantage of creating defects with precise spatial control. Therefore, we hypothesize that a laser beam can enable precise spatial control over the photoetching of MoS_2 with subsequent nanoparticle deposition at specific locations. To verify our hypothesis, a 532 nm laser was employed to irradiate MoS_2 in air to create defects selectively. Laser-carved MoS_2 flakes were then exposed to $FeCl_3$ under halogen lamp illumination, resulting in nanostructure growth in the etched regions (the process described in section 2.1). This process is schematically illustrated in Fig. 3(a).

Fig. 3(b–e) illustrates the progression of etching at laser-carved spots by optical and AFM imaging. Optical images show an increased diameter of etched regions; the photoetching process started from the laser-carved spots. AFM images evidence remarkable changes in height and surface roughness. Before immersion in $FeCl_3$, the diameter of laser-formed spots was about 650 nm, close to the laser beam diameter of approximately 800 nm. After photoetching, the diameter of the laser-carved area increased to 5 μm (see Fig. 3(d) and (f)). Additionally, the root mean square roughness in the etched area increased to 6.5 ± 1.5 nm, compared to 1.3 ± 0.8 nm

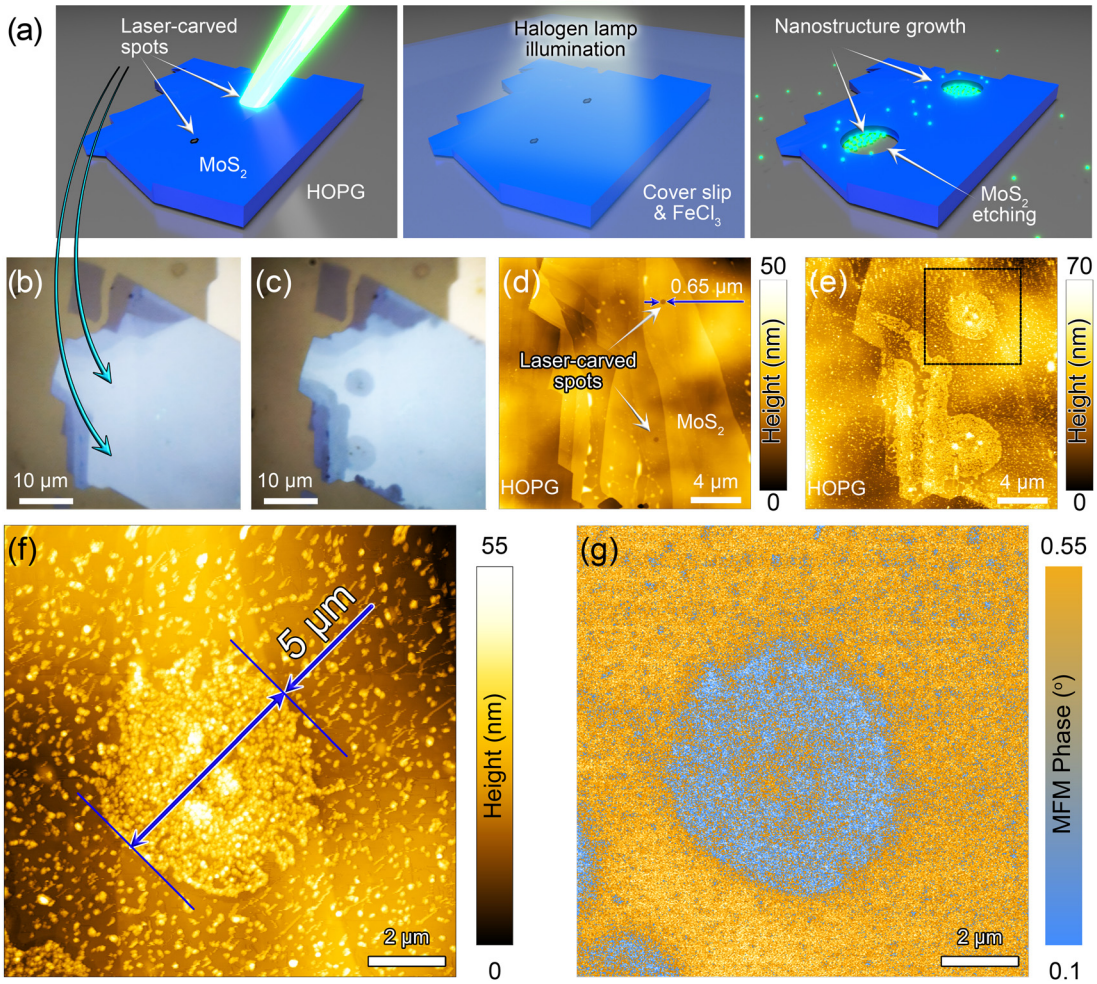

Fig. 3 (a) Schematic of the process: laser carving creates defects in MoS_2 on HOPG, followed by $FeCl_3$ immersion and illumination resulting in nanostructure growth in etched regions. (b and c) Optical images of MoS_2 before and after photoetching, showing an increase in the laser-etched region diameter. (d and e) AFM images of laser spots before (~650 nm) and after (~5 μm) etching, with increased surface roughness (6.5 ± 1.5 nm) in etched areas. (f) High-resolution AFM of the etched region. (g) MFM phase image shows enhanced magnetic contrast, confirming the formation of magnetic iron oxide nanoparticles.

before etching due to the photoetching and nanoparticle deposition. The contrast difference in the MFM phase image demonstrates differences in magnetic properties between the non-magnetic MoS_2 and the functionalized/etched spot (Fig. 3(g)), indicating the deposition of magnetic nanoparticles, likely iron oxide, that is consistent with EDX data presented in Fig. S7.†

We showed that laser-engraving technology enabled to selectively control the creation of nanoparticles in specific regions, providing a way to add magnetic properties to MoS_2 at predefined locations and to achieve spatially controlled photoetching.

2.3. Boosting the ROS production by a Fenton-like reaction with $CuSO_4$ for MoS_2 photoetching

We wanted to explore whether our approach could be extended to Fenton reactions using metal ions other than iron. In this context, Cu^{2+} ions, which are commonly employed for ROS generation in Fenton-like reactions,[38,39] prompted us to investigate the feasibility of selective MoS_2 photoetching in $CuSO_4$ solution. Cu^+ regeneration can be accomplished through the absorption of photoexcited electrons in the semiconductor by Cu^{2+}, reducing it to Cu^+, as shown in eqn (7)[40] or by the reaction with $^{\bullet}O_2^-$ (eqn (8)):

$$\begin{aligned} &Cu^{2+} + e^- \rightarrow Cu^+ \text{ at } 0.153\,\text{V } vs.\ \text{SHE} \\ &(-4.59\,\text{eV } vs.\ E_{vac}) \text{ at pH} = 7 \end{aligned} \tag{7}$$

$$Cu^{2+} + {}^{\bullet}O_2^- \rightarrow Cu^+ + O_2, \quad k = 6.6 \times 10^8\ M^{-1}\ s^{-1} \tag{8}$$

$$Cu^+ + H_2O_2 \rightarrow Cu^{2+} + OH^- + {}^{\bullet}OH, \quad k = 4 \times 10^5\ M^{-1}\ s^{-1} \tag{9}$$

The Cu^+ reacts with H_2O_2 and O_2 in a Fenton-like reaction to produce $^{\bullet}OH$ radicals, as described in the following reactions (9).[41]

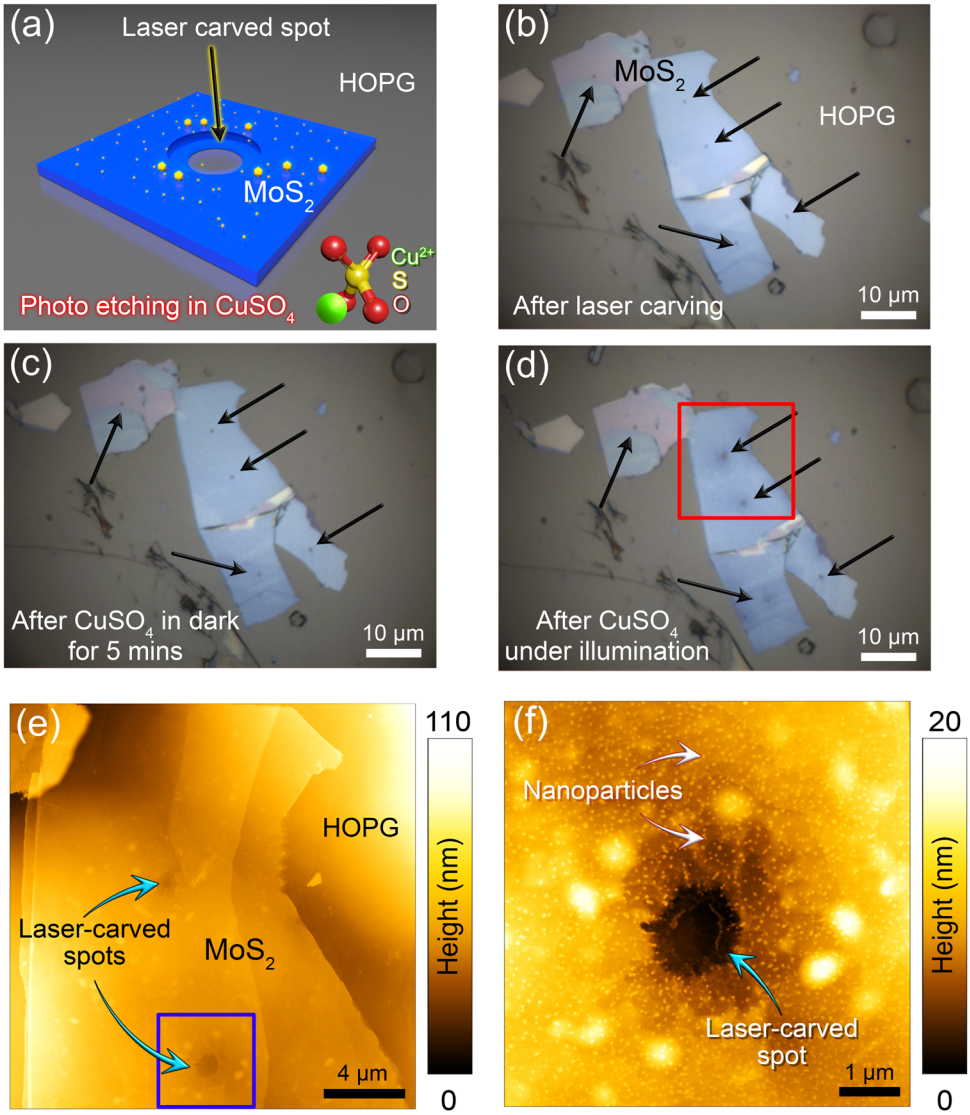

Fig. 4 (a) Schematic of photo-etching in $CuSO_4$ at laser-carved spots on MoS_2/HOPG under halogen lamp illumination. (b–d) Optical images: (b) after laser carving, (c) after $CuSO_4$ exposure in the dark, and (d) after illumination, showing selective etching at defects. (e and f) AFM images: (e) etched regions on MoS_2 and (f) zoomed-in area showing Cu_2O nanoparticles, formed *via* Fenton-like reactions.

Fig. 4(a) shows a schematic of the selective photoetching process in $CuSO_4$ at laser-carved spots on MoS_2. Optical images (see Fig. 4(b)–(d)) confirm the etching of MoS_2 after exposure to $CuSO_4$ under halogen lamp illumination, in contrast to the absence of change in the optical image without illumination. The photoetching selectively occurred at the MoS_2/HOPG/$CuSO_4$ interface or laser-carved defects. AFM images in Fig. 4(e) and (f) prove the photoetching in $CuSO_4$ solutions. Nevertheless, we observed Cu_2O nanoparticles resulting from Fenton-like reactions, as confirmed by Raman spectroscopy results showing the peaks from Cu_2O in the etched region (see Fig. S14†). The etching efficiency of MoS_2 in $CuSO_4$ is lower than that in the $FeCl_3$ solution (see Fig. S12†), which may be attributed to the lower activity of Cu^{2+} ions.[42]

Given the light-driven nature of this process, our work opens perspectives for scalability and the use of white light illumination to drive ROS production for selective photoetching of multilayer MoS_2 to few-layer MoS_2 with high defect density and simultaneous metal oxide nanoparticle deposition. This approach could benefit applications such as catalyst creation for pollution control, including wastewater treatment.

2.4. Practical applications: enhanced HER performance

MoS_2 is a promising non-noble stable metal catalyst for the HER.[43] To demonstrate the practical applications of our photochemical etching method based on the Fenton reaction, we evaluated the HER performance of MoS_2-based materials. The HER activity was assessed using electrochemical measurements under alkaline conditions (1 M KOH). Linear sweep voltammetry (LSV) curves for the graphite electrode (GE), the GE with MoS_2 (GE/MoS_2), and the GE/MoS_2 treated with $FeCl_3$ in

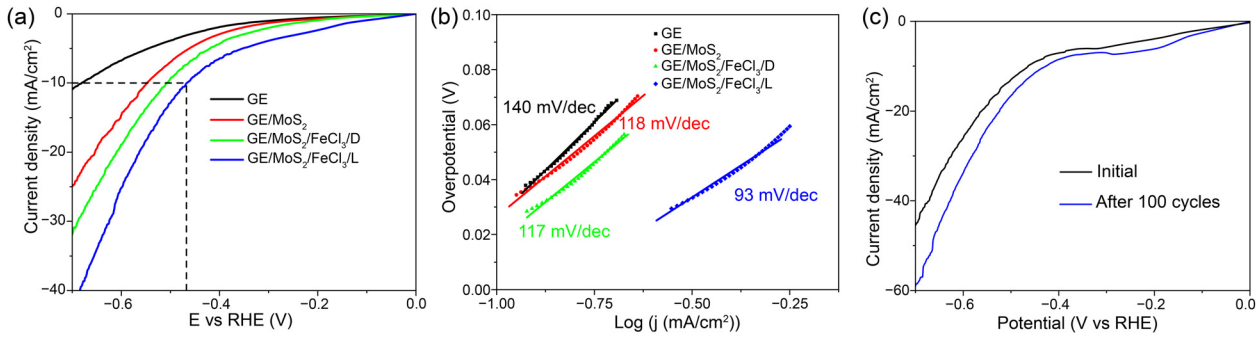

Fig. 5 (a) LSV curves of the GE, GE/MoS_2, GE/MoS_2/$FeCl_3$/D, and GE/MoS_2/$FeCl_3$/L samples. (b) Tafel slopes derived from the curves in (a). (c) Stability test of the GE/MoS_2/$FeCl_3$/L sample. The catalyst is still stable after 100 cycles.

the dark (GE/MoS_2/$FeCl_3$/D) and under halogen lamp illumination (GE/MoS_2/$FeCl_3$/L) are shown in Fig. 5. After depositing MoS_2 on the GE, the HER performance increases, indicating the high catalytic activity of MoS_2. Subsequent treatment of GE/MoS_2 with $FeCl_3$ under dark conditions further improves performance, as reflected by the high current density of GE/MoS_2/$FeCl_3$/D (see Fig. 5(a)), likely due to iron oxide particle deposition. The sample prepared under illumination, GE/MoS_2/$FeCl_3$/L, shows the best performance of all, as evidenced by an overpotential shift to a less negative value and a significantly higher current density across the entire potential range, indicating a more efficient hydrogen generation process. Defect creation and iron oxide nanoparticle formation *via* the photochemical Fenton reaction lead to the formation of additional active sites for the HER, resulting in a potential shift from −0.7 V (GE) to −0.47 V (GE/MoS_2/$FeCl_3$/L) at a current density of 10 mA cm^{-2}. Thus, our simple and scalable approach for modifying the electrode surface effectively improves the electrocatalytic performance of the electrode for the HER.

To understand the elementary steps in the HER, Tafel slopes are derived from linear portions of Tafel plots fitted to the equation $\eta = b \times \log(j) + a$, where η is the overpotential (V), j is the current density (mA cm^{-2}), and b is the Tafel slope in mV dec^{-1}. Three possible reaction steps governing HER kinetics are as follows: the Volmer reaction ($b \approx 120$ mV), the Heyrovsky reaction ($b \approx 40$ mV), and the Tafel reaction ($b \approx 30$ mV).[44] For the GE, GE/MoS_2, GE/MoS_2/$FeCl_3$/D, and GE/MoS_2/$FeCl_3$/L, the Tafel slopes are 140, 118, 117, and 93 mV dec^{-1}, respectively (see Fig. 5(b)). The GE/MoS_2/$FeCl_3$/L exhibits the smallest Tafel slope of 83 mV dec^{-1}, indicating a Volmer–Heyrovsky reaction.[45] Additionally, after 100 HER cycles, the GE/MoS_2/$FeCl_3$/L sample maintained consistent HER performance, demonstrating good electrochemical stability (see Fig. 5(c)).

3. Conclusion

This work presents a simple, novel, scalable, and environmentally friendly approach for the spatially controlled etching and nanoparticle functionalization of multilayer MoS_2 to few-layer MoS_2 with high defect density, achieved by low-intensity halogen lamp illumination in $FeCl_3$ and $CuSO_4$ solution. Based on Fenton reactions, this method, validated by Raman spectroscopy, scanning probe microscopy methods, optical microscopy, scavenging experiments, and scanning electron microscopy with elemental mapping, enables light-driven MoS_2 thinning, defect creation and nanoparticle functionalization. We elucidated the mechanism behind photochemical defect formation and thinning based on the generation of strongly oxidizing $^{\bullet}OH$ radicals through Fenton reactions. Furthermore, we demonstrated the spatially selective functionality through the simultaneous growth of magnetic nanoparticles at predetermined locations using laser engraving technology. Our approach improved MoS_2 performance in the HER by introducing defects and metal oxides. In conclusion, this work provides a novel strategy for thinning of MoS_2 to a monolayer, introducing defects, and achieving metal functionalization in a single simple processing step compatible with large-scale production, offering potential benefits for applications in (photo)catalysis and optoelectronics applications.

4. Materials and methods

4.1. Materials

MoS_2 flakes were obtained through mechanical exfoliation of natural bulk 2H-MoS_2 crystals and subsequently deposited on four substrates: highly oriented pyrolytic graphite (HOPG) (NT-MDT, Russia), Si/SiO_2, indium tin oxide (ITO), and polydimethylsiloxane (PDMS) (Gel@Pak, Korea). The $FeCl_3$ salt was purchased from Sigma-Aldrich and used without further purification.

4.2. Atomic force microscopy

Surface morphology and electronic properties were characterized using an NTEGRA PRIMA atomic force microscope (NT-MDT, Russia). Topography and Kelvin probe force microscopy (KPFM) measurements were performed using NSG10 and NSG10/Pt tips (NT-MDT, Russia), while magnetic force microscopy was conducted using MFM01 tips (NT-MDT, Russia).

4.3. Photoluminescence and Raman spectroscopy

Photoluminescence (PL) and Raman spectra were recorded using a Raman spectrometer (NT-MDT SI, Russia). All spectra were recorded using a 532 nm laser with a 100× objective with 1800 or 150 mm^{-1} gratings for Raman and PL spectra, respectively. Laser power after the objective was 0.1 mW.

4.4. Scanning electron microscopy (SEM)

SEM images and elemental maps were obtained using an *in situ* analytical scanning electron microscope, TESCAN MAGNA (TESCAN, Czech Republic), at 10 kV.

4.5. Laser carving for defect creation

Laser carving of MoS_2 flakes was performed using a 532 nm laser with the power of 12 mW after a 100× objective in air.

4.6. Photoetching experiment

A 10 μL drop of the aqueous solution of the investigated salt was deposited onto the MoS_2 flake and covered with a glass coverslip to ensure uniform solution distribution and enable optical imaging. Samples were illuminated using a halogen lamp, Schott ACE I A20510 (Schott, Germany), at the power of 22.5 W, focused through a 100× objective. The spectrum of the halogen lamp is provided in Fig. S4.† After illumination, the coverslip was removed, and samples were rinsed with distilled water. The terms of photooxidation and photoetching are the same in our case, as photooxidation leads to thinner MoS_2 flakes.

4.7. Electron paramagnetic resonance (EPR) spectroscopy experiments

5,5-Dimethyl-1-pyrroline-*N*-oxide (DMPO) was used as a spin-trapping agent. MoS_2 was dispersed in water to obtain a concentration of 2.5 mg mL^{-1}. This dispersion was mixed at a 1 : 1 volume ratio with 0.1 mM $FeCl_3$. This concentration of $FeCl_3$ minimizes interference with DMPO. A high amount of DMPO (0.10 g) was added to stabilize radicals and limit oxidation by Fe^{3+}.

4.8. $^{\bullet}OH$ scavenging experiment

The same experiment as the photo-etching experiment was conducted using a 10 μL drop of a mixed solution containing 1 mM $FeCl_3$/98% 2-isopropanol (IPA) at a volume ratio of 1 : 1.

4.9. pH measurement experiment

The pH values of 0.05 M MoS_2 dispersion, 0.05 M $FeCl_3$ solution and 0.05 M MoS_2/0.05 M $FeCl_3$ dispersion were measured by a colorimetric method using litmus (Aquanatura, Germany).

4.10. Electrochemical measurements

A graphite electrode (GE) was prepared following a previously reported protocol.[46] The GE/MoS_2 working electrode was prepared by drop-casting 10 μL of MoS_2 solution (0.01 g of MoS_2 per mL of ethanol) onto the GE and allowing it to dry. Subsequently, a small volume (<10 μL) of chloroform was applied to improve adhesion, followed by drying at room temperature (~10 minutes) and then at 49 °C for an additional 10 minutes.

GE/MoS_2/$FeCl_3$/D was prepared by immersing the GE/MoS_2 electrode in 1 mM $FeCl_3$ for 15 minutes. GE/MoS_2/$FeCl_3$/D was prepared by immersing the GE/MoS_2 electrode in 1 mM $FeCl_3$ under halogen lamp illumination for 15 minutes. Electrochemical HER activity and stability tests were conducted using a three-electrode cell configuration connected to a potentiostat (Corrtest, China). An Ag/AgCl (3.0 M NaCl) and a platinum wire were used as reference and counter electrodes, respectively. HER performance was evaluated in aqueous 1.0 M KOH (pH 13.7). Cyclic voltammetry (CV) and LSV were performed by scanning from −0.9 V to −1.8 V *vs.* Ag/AgCl at a scan rate of 25 mV s^{-1}. All potentials were converted into the reversible hydrogen electrode (RHE) scale using the following formula: $E_{RHE} = E(Ag/AgCl) + 0.059\ pH + 0.209$. Electrochemical stability was tested over 100 CV cycles across the specified potential range.

Author contributions

Tuan-Hoang Tran: methodology, investigation, formal analysis, visualization, writing – original draft, and review & editing. Raul D. Rodriguez: conceptualization, methodology, investigation, formal analysis, visualization, writing – original draft, and review & editing. Aura S. Garcia: methodology, investigation, formal analysis, visualization, writing – original draft, and review & editing. Tao Zhang: methodology and review & editing. Qiang Ma: investigation and review & editing. Ranran Wang: conceptualization, funding acquisition, and review & editing. Evgeniya Sheremet: conceptualization, formal analysis, methodology, funding acquisition, writing – original draft and review & editing.

Data availability

The data that support the findings of this study are available from the corresponding author, Raul D. Rodriguez, upon reasonable request.

Conflicts of interest

The authors declare that they have no known competing financial interests or personal relationships that could have appeared to influence the work reported in this paper.

Acknowledgements

We acknowledge funding by RSF Grant No. 23-42-00081. Ranran Wang thanks support from the National Natural Science Foundation of China (Grant No. 62261136551). Q. M. is thankful to the China Postdoctoral Science Foundation (2024M753340) and the Postdoctoral Fellowship Program of CPSF (Grant Number GZC20232796) for the financial support. The authors also gratefully acknowledge Maksim Fatkullin and Pavel Petunin from Tomsk Polytechnic University for fruitful discussions and comments on the manuscript.

References

1 A. Splendiani, L. Sun, Y. Zhang, T. Li, J. Kim, C.-Y. Chim, G. Galli and F. Wang, *Nano Lett.*, 2010, **10**, 1271–1275.
2 J. Jiang, Z. Chen, Y. Hu, Y. Xiang, L. Zhang, Y. Wang, G.-C. Wang and J. Shi, *Nat. Nanotechnol.*, 2021, **16**, 894–901.
3 Y. Teng, H. Zhao, Z. Zhang, Z. Li, Q. Xia, Y. Zhang, L. Zhao, X. Du, Z. Du, P. Lv and K. Świerczek, *ACS Nano*, 2016, **10**, 8526–8535.
4 A. Taffelli, S. Dirè, A. Quaranta and L. Pancheri, *Sensors*, 2021, **21**(8), 2758.
5 Z. Li, X. Meng and Z. Zhang, *J. Photochem. Photobiol., C*, 2018, **35**, 39–55.
6 D. Wei, B. Wu, Y. Guo, G. Yu and Y. Liu, *Acc. Chem. Res.*, 2013, **46**, 106–115.
7 S. Bai, N. Zhang, C. Gao and Y. Xiong, *Nano Energy*, 2018, **53**, 296–336.
8 H. Wang, C. Tsai, D. Kong, K. Chan, F. Abild-Pedersen, J. K. Nørskov and Y. Cui, *Nano Res.*, 2015, **8**, 566–575.
9 P. Zhang, H. Xiang, L. Tao, H. Dong, Y. Zhou, T. S. Hu, X. Chen, S. Liu, S. Wang and S. Garaj, *Nano Energy*, 2019, **57**, 535–541.
10 S. H. Choi, S. J. Yun, Y. S. Won, C. S. Oh, S. M. Kim, K. K. Kim and Y. H. Lee, *Nat. Commun.*, 2022, **13**, 1484.
11 K. K. Amara, L. Chu, R. Kumar, M. Toh and G. Eda, *APL Mater.*, 2014, **2**, 092509.
12 Y. Liu, H. Nan, X. Wu, W. Pan, W. Wang, J. Bai, W. Zhao, L. Sun, X. Wang and Z. Ni, *ACS Nano*, 2013, **7**, 4202–4209.
13 B.-C. Tran-Khac, R. M. White, F. W. DelRio and K.-H. Chung, *Nanotechnology*, 2019, **30**, 275302.
14 D. Ghim, P.-I. Chou, S. H. Chae and Y.-S. Jun, *Environ. Sci. Technol.*, 2021, **55**, 13759–13769.
15 L. Li, Q. Han, L. Wang, B. Liu, K. Wang and Z. Wang, *Chem. Eng. J.*, 2022, **440**, 135866.
16 E. Brillas, I. Sirés and M. A. Oturan, *Chem. Rev.*, 2009, **109**, 6570–6631.
17 X. Wang, X. Zhang, Y. Zhang, Y. Wang, S.-P. Sun, W. D. Wu and Z. Wu, *J. Mater. Chem. A*, 2020, **8**, 15513–15546.
18 M. Pera-Titus, V. García-Molina, M. A. Baños, J. Giménez and S. Esplugas, *Appl. Catal., B*, 2004, **47**, 219–256.
19 T. Liu, Z. Pan, J. J. M. Vequizo, K. Kato, B. Wu, A. Yamakata, K. Katayama, B. Chen, C. Chu and K. Domen, *Nat. Commun.*, 2022, **13**, 1034.
20 R. Zhang, Z. Liu and T. Chen, *Photochem. Photobiol.*, 2024, **100**, 1745–1758.
21 H. Song, L. Wei, C. Chen, C. Wen and F. Han, *J. Catal.*, 2019, **376**, 198–208.
22 T.-H. Tran, R. D. Rodriguez, N. E. Villa, S. Shchadenko, A. Averkiev, Y. Hou, T. Zhang, A. Matkovic and E. Sheremet, *J. Colloid Interface Sci.*, 2024, **654**, 114–123.
23 S. Gligorovski, R. Strekowski, S. Barbati and D. Vione, *Chem. Rev.*, 2015, **115**, 13051–13092.
24 T.-H. Tran, R. D. Rodriguez, D. Cheshev, N. E. Villa, M. A. Aslam, J. Pešić, A. Matković and E. Sheremet, *Appl. Surf. Sci.*, 2022, **604**, 154585.
25 H. Nan, Z. Wang, W. Wang, Z. Liang, Y. Lu, Q. Chen, D. He, P. Tan, F. Miao, X. Wang, J. Wang and Z. Ni, *ACS Nano.*, 2014, **8**, 5738–5745.
26 S. Mouri, Y. Miyauchi and K. Matsuda, *Nano Lett.*, 2013, **13**, 5944–5948.
27 L. Chen, M. Arshad, Y. Chuang, C.-W. Chen and C.-D. Dong, *Mater. Sci. Semicond. Process.*, 2023, **167**, 107780.
28 S.-S. Wu, T.-X. Huang, K.-Q. Lin, X. Yao, J.-T. Hu, D.-L. Tang, Y.-F. Bao and B. Ren, *2D Mater.*, 2019, **6**, 045052.
29 G. A. Ermolaev, Y. V. Stebunov, A. A. Vyshnevyy, D. E. Tatarkin, D. I. Yakubovsky, S. M. Novikov, D. G. Baranov, T. Shegai, A. Y. Nikitin, A. V. Arsenin and V. S. Volkov, *Npj 2D Mater. Appl*, 2020, DOI: **10.1038/s41699-020-0155-x**.
30 H. Li, Q. Zhang, C. C. R. Yap, B. K. Tay, T. H. T. Edwin, A. Olivier and D. Baillargeat, *Adv. Funct. Mater.*, 2012, **22**, 1385–1390.
31 S. Fu, K. Kang, K. Shayan, A. Yoshimura, S. Dadras, X. Wang, L. Zhang, S. Chen, N. Liu, A. Jindal, X. Li, A. N. Pasupathy, A. N. Vamivakas, V. Meunier, S. Strauf and E.-H. Yang, *Nat. Commun.*, 2020, **11**, 2034.
32 N. Kang, H. P. Paudel, M. N. Leuenberger, L. Tetard and S. I. Khondaker, *J. Phys. Chem. C*, 2014, **118**(36), 21258–21263.
33 H. Li, K. Yu, C. Li, Z. Tang, B. Guo, X. Lei, H. Fu and Z. Zhu, *Sci. Rep.*, 2015, **5**, 18730.
34 L. Yu, Y.-H. Lee, X. Ling, E. J. G. Santos, Y. C. Shin, Y. Lin, M. Dubey, E. Kaxiras, J. Kong, H. Wang and T. Palacios, *Nano Lett.*, 2014, **14**, 3055–3063.
35 T. Liang, W. G. Sawyer, S. S. Perry, S. B. Sinnott and S. R. Phillpot, *J. Phys. Chem. C*, 2011, **115**, 10606–10616.
36 Z. Wang, Y.-J. Zhang, M. Liu, A. Peterson and R. H. Hurt, *Nanoscale*, 2017, **9**, 5398–5403.
37 Y. Shi, J.-K. Huang, L. Jin, Y.-T. Hsu, S. F. Yu, L.-J. Li and H. Y. Yang, *Sci. Rep.*, 2013, **3**, 1839.
38 T. T. M. Nguyen, H.-J. Park, J. Y. Kim, H.-E. Kim, H. Lee, J. Yoon and C. Lee, *Environ. Sci. Technol.*, 2013, **47**, 13661–13667.
39 A. N. Pham, G. Xing, C. J. Miller and T. D. Waite, *J. Catal.*, 2013, **301**, 54–64.
40 P. Vanysek, *CRC handbook of chemistry and physics*, 2000, vol. 8, pp. 8–33.
41 J. Li, A. N. Pham, R. Dai, Z. Wang and T. D. Waite, *J. Hazard. Mater.*, 2020, **392**, 122261.
42 H. Lee, J. Seong, K.-M. Lee, H.-H. Kim, J. Choi, J.-H. Kim and C. Lee, *J. Hazard. Mater.*, 2018, **344**, 1174–1180.
43 Y. Cao, *ACS Nano*, 2021, **15**, 11014–11039.
44 T. Shinagawa, A. T. Garcia-Esparza and K. Takanabe, *Sci. Rep.*, 2015, **5**, 13801.
45 B. Tian, L. Sun, Z. Zeng and D. Ho, *J. Mater. Chem. A*.
46 A. M. Surkov, R. G. Queiroz, R. S. Rinco, A. G. Rios, I. G. R. Gutz, A. L. B. Baccaro and L. Angnes, *Talanta*, 2021, **223**, 121780.

